We are IntechOpen, the world's leading publisher of Open Access books
Built by scientists, for scientists

6,900
Open access books available

185,000
International authors and editors

200M
Downloads

Our authors are among the

154
Countries delivered to

TOP 1%
most cited scientists

12.2%
Contributors from top 500 universities

CLARIVATE ANALYTICS
BOOK CITATION INDEX
INDEXED

WEB OF SCIENCE™

Selection of our books indexed in the Book Citation Index
in Web of Science™ Core Collection (BKCI)

Interested in publishing with us?
Contact book.department@intechopen.com

Unsteady Computational and Experimental Fluid Dynamics Investigations of Aerodynamic Loads of Large Optical Telescopes

Mahmoud Mamou[1], Youssef Mébarki[1] and Ali Tahi[2]

[1]Aerodynamics Laboratory, Institute for Aerospace Research, National Research Council
Ottawa, Ontario,
[2]Département d'Aéronautique, Faculté des Sciences de l'Ingénieur,
Université Saad Dahlab-Blida,
[1]Canada
[2]Algérie

1. Introduction

The present chapter includes a comprehensive literature review of flow simulations and measurements of aerodynamic loads on large optical telescopes, and a discussion on a recent computational fluid dynamics (CFD) investigation, supported by wind tunnel measurements. The investigation was performed at the National Research Council of Canada (NRC) and was focused mainly on predicting and measuring unsteady wind loads on a scaled wind tunnel model of a Very Large Optical Telescope (VLOT), and on a VLOT full-scale model housed within spherical enclosures.

Optical telescopes are usually housed in confined enclosures with apertures to limit buffeting problems caused by environmental disturbances such as wind and onsite thermal plumes or by the combined effect. In other words, the enclosures enhance the telescope pointing and tracking performance and also preserve the primary mirror optical shape by minimizing or reducing the unsteady wind loads and air circulation fluctuations inside the enclosure.

Most of the present generation telescopes are equipped with relatively small primary mirror areas that limit the light-gathering power and angular resolution. This obviously causes a detrimental effect and restrictions on the telescope performance in capturing details of distant celestial objects, which are key elements for understanding the origin of the universe. To overcome this limitation, astrophysicists are building much larger optical telescopes to allow large mirror reflecting areas. Consequently, massive and stiff supporting structures are required. As the telescopes grow in size, structural buffeting, unsteady wind loads, thermal mass, and other issues become crucial factors that must be considered in the early design phases.

The enclosure requires an opening without shielding to avoid smearing of light and electromagnetic waves, and diffraction. The boundary layer flow that starts to build up from the stagnation point on the enclosure surface up to the upstream edge of the opening, must detach and by doing so forms a free strong shear layer across the opening. Under some flow conditions, the shear layer becomes unstable and rolls up into a series of strong and distinct vortices, which impinge against the aft edge of the opening. As a result, acoustic waves are

generated, affecting the flow inside the enclosure (unsteady pressure loads) and over the opening (possible shear layer excitation). When the acoustic waves arrive near the leading edge of the opening, where the shear layer starts to build up, they excite and strengthen the newly formed vortices, which could result in aeroacoustic coupling. A strong pressure fluctuation is thus induced inside the enclosure, which in turn contributes to significant dynamic loads on the telescope structure. As the size of telescopes increases, their structural natural frequency is shifted to lower values closer to the wind loading frequencies, which collectively may impart significant structure buffeting on the telescope components.

This chapter focuses mainly on the CFD simulations of unsteady flows past a very large optical telescope structure that were conducted at the National Research Council. The CFD simulations were performed using the Lattice Boltzmann method as implemented in the commercial PowerFLOW™ solver. Unsteady viscous flow solutions were computed for various zenith and azimuth angles. The CFD simulations were performed assuming fully turbulent flows past the enclosure. For the full-scale telescope enclosure, the Reynolds number is large (about 5×10^7) and, according to Achenbach's results for sphere flow (1974), the assumption of fully turbulent flow can be justified.

As a high Reynolds number test was beyond the scope of this investigation, a scaled model was tested at moderate Reynolds number (about 5×10^5) to provide a basis for planning future tests. Although the flow conditions were strictly not matched, it was thought that the flow unsteadiness inside the enclosure would not be strongly affected by the complex flow phenomena around the exterior surface of the enclosure. Therefore, the experimental results were still expected to shed some light on the internal flow field. The validity of this assumption could be established in the future by performing more comprehensive tests, or considering advanced CFD codes allowing for automatic prediction of flow transition and separation.

The objective of the CFD investigation was to assess the capabilities of a flow solver in predicting some of the flow properties inside and outside the telescope enclosure by mimicking the wind tunnel flow conditions. Correlations were obtained between the CFD and wind tunnel (WT) data in terms of the mean pressure coefficients on the enclosure and on the primary mirror surfaces, and their standard deviations. Power spectral density analyses were also carried out for a number of pressure signals collected on the primary mirror surface. Also, infrared measurements were performed to characterize the boundary layer flow behavior around the telescope enclosure in order to determine the transition and flow separation locations, which depended on the Reynolds number, telescope roughness, turbulence level and telescope orientations. The CFD solutions affirmed that the flow inside and outside the enclosure was unsteady and massively separated on the back of the enclosure.

2. Review of flow simulations on large telescopes

The astrophysics community is building larger and larger telescopes, such as the Thirty Meter Telescope (TMT), in order to study the universe in greater detail (Angeli *et al.*, 2004). For such large structures, the unsteady wind loading is becoming an important factor in the telescope design phase. The wind flow around and inside the telescope enclosure can lead to many direct undesirable effects upon the "seeing" attributes of the primary mirror. The seeing factor describes how much the turbulence of the earth's atmosphere and the flow inside the telescope enclosure perturbs the images of stars as seen through the telescope. An increase in the "seeing" factor is generally associated with a degradation of the optical

performance of the telescope. The induced unsteady pressure loads on the telescope components lead to a dynamic structure deformation, causing wind buffeting that, owing to the large size of the telescope, directly affects the primary mirror as well as the secondary mirror assembly, which is usually exposed to relatively higher wind speeds and shear layer unsteadiness near the enclosure opening.

The application of CFD to predict flows and pressure loads on telescope structures can provide critical and detailed data for the design of future large optical telescopes. Most of the flow phenomena that affect the mirror seeing can be assessed by CFD within an acceptable level of accuracy.

Several CFD studies have been reported for ground-based telescopes. De Young (1996) performed time-independent airflow simulations inside the Gemini telescope enclosure. The author found that venting (airflow through vents) was most effective means of influencing flow directions inside the enclosure; particularly near the vents and across the primary mirror surface. Turbulence was present for different wind conditions and orientations; however, it was worst when the enclosure opening was facing the wind. The author also identified a strong pressure gradient across the primary mirror for different wind conditions. Similarly, using CFD, Vogiatzis *et al*. (2004) estimated the effect of unsteady wind loading on the performance of extremely large telescopes (ELT). The CFD predictions were validated against WT measurements. The study showed the existence of an unstable shear layer over the opening that caused significant pressure fluctuations inside the enclosure. The power spectral density of the normalized velocity signal, measured near the enclosure opening, showed the existence of different oscillatory mode frequencies, which agreed well with experimental data. De Young and Vogiatzis (2004) simulated steady-state airflow past very large optical telescope enclosures. The simulations were performed for an extremely large typical empty telescope enclosure, as well as for the more specific Gemini South telescope mounted on the summit of Mount Cerro Pachon. The authors reported only qualitative flow pattern results to demonstrate the feasibility and ability of CFD to simulate and predict pressure loads inside and outside the telescope enclosure.

Cho *et al*. (2001) investigated wind-buffeting effects on the Gemini 8-m primary mirror. The measurements were performed under onsite mountaintop wind conditions. Pressure data were obtained at various taps installed on the primary mirror, and the wind velocity and direction were measured at several locations inside and outside the enclosure. To assess the dynamic response of the telescope, the time history of the pressure data was used to calculate the primary mirror deformation using a finite-element method. Angeli *et al*. (2002) studied experimentally the characteristics of wind loading on the Gemini telescope. The authors found that the pressure fluctuations on the primary mirror were extremely pronounced when the mirror was pointing into the wind with a small bandwidth of the wind loading. Cho *et al*. (2003) also reported a similar study of the wind loading on the Gemini telescope. They found that the pressure fluctuations over the primary mirror were significant; however, the global wind force on the mirror was negligibly small. The average pressure on the primary mirror was mainly controlled by the airflow around the enclosure opening, and the fluctuations were caused by the turbulence generated by the enclosure structures. Quattri *et al*. (2003) performed full-scale flow simulations of wind loading on the 100-m OWL telescope using commercial CFD software. The study focused on the wind loads acting on the primary mirror with the loads predominantly induced by a nearby building situated upstream of telescope structure. Pressure signals collected at different points on the mirror surface showed that the wind pressure load at low frequencies was

reduced by the building; however, the high frequency wind pressure components increased under these conditions. Angeli *et al*. (2004) presented an integrated approach for the necessary modeling tools to estimate the performance of the TMT, which is an upgraded version of the VLOT. Among these tools, the authors emphasized the role of CFD in predicting the wind loading and buffeting, which are more crucial during the conceptual design phase of the telescope. As shown in Fig. 1, a flow simulation was performed past a generic telescope. The flow is highly unsteady, especially over the slit and behind the enclosure, and it was observed that the air pressure inside the dome is dominated by the lowest frequency of the acoustic waves generated by the unsteady free shear layer interaction with the dome slit edge.
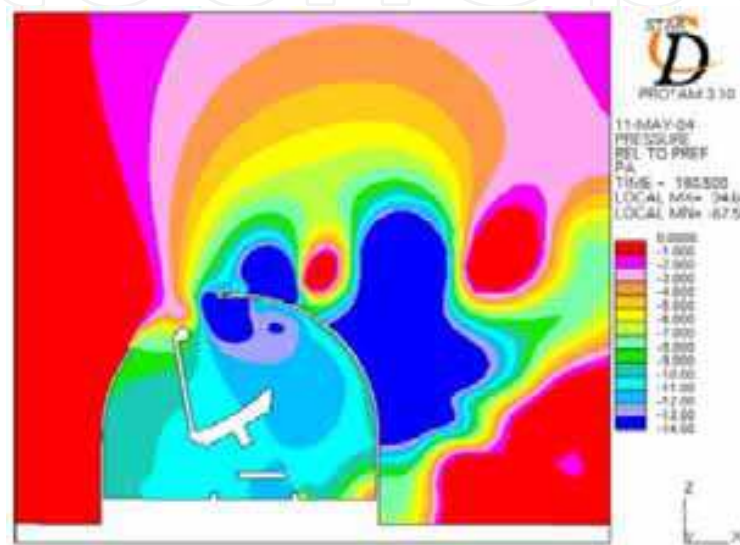

Fig. 1. A snapshot of the pressure field in and around the generic ELT dome with a Giant Segmented Mirror Telescope model inside (Angeli *et al*. (2004)

Riewaldt *et al*. (2004) also carried out an interesting and thorough wind tunnel investigation for an extremely large telescope with a 50-m primary mirror diameter. The investigation was performed on a 1:200-scale model in the boundary layer wind tunnel at the National University in Galway, Ireland. Pressure signals were measured at various locations on the primary mirror and on the enclosure. This particular study included a number of different telescope configurations: an empty enclosure, a telescope unit on its own, and a combined telescope and enclosure configuration. Aerodynamic forces and moments acting on the enclosure and on the telescope primary mirror were also measured. The authors concluded that under nominal wind conditions (12 m/s), the wind produced a large mean pressure load and significant pressure fluctuations on the primary mirror surface. In addition to the above studies, Pottebaum and MacMynowski (2006) conducted WT measurements of the flow inside an empty generic telescope enclosure with a rectangular opening. Smoke and tuft visualizations were performed to illustrate the flow patterns inside and around the enclosure. Digital particle image velocimetry data were obtained on a vertical plane near the enclosure opening to estimate the mean flow velocity and the kinetic energy fluctuations. The experimental observations and measurements again revealed the existence of a strong shear layer that formed over the enclosure opening when it was pointing into the wind. Different oscillatory mode frequencies were detected. When the enclosure opening was facing downstream, the flow was driven inside the enclosure with less rigorous unsteady

flow structures, because the mechanisms for coupling has been removed. Drilling some vents around the enclosure structure, appeared to weaken the shear layer and the amplitudes of the oscillatory modes were dampened.

MacMynowski *et al.* (2006) documented the effect of wind load and buffeting on ground-based telescopes and identified the sources that lead to better understanding the wind flow characteristics inside the telescope enclosure and past its aperture. One of the sources relies on CFD analyses using current state-of-the-art numerical techniques and advanced turbulence models. Non-vented and vented enclosure configurations were analyzed. For a non-vented enclosure, the shear layer modes are strong for given orientations, as observed in wind-tunnel and predicted by CFD results; however they are not the most important source of unsteadiness of wind loads on the telescope components. For a vented enclosure, the shear layer was weakened, resulting in low-amplitude modes. The authors reported difficulties using CFD to predict accurately the flow turbulence behavior along the telescope axis, when compared to experiment.

Quattri *et al.* (2008) performed WT measurements to characterize the wind turbulence structure and intensity inside two types of telescope enclosures with different screen positions. WT data were obtained for various wind speeds and enclosure orientations, which will certainly serve for future CFD code validations.

For airborne telescopes, Srinivasan (1997) and (2000) used a combined CFD and experimental approach for the airborne Stratospheric Observatory for Infrared Astronomy (SOFIA) to investigate the challenges related to aerodynamic and aeroacoustic problems. The telescope was housed in an open built-in cavity on a Boeing 747 aircraft fuselage. Comparisons with CFD results obtained under the wind tunnel conditions showed fairly good agreement for sound pressure levels and power spectra at various locations within the cavity and on the telescope. However, the power spectral density of the pressure signals on the telescope surface showed that the agreement between CFD and experiment was achieved within a narrow frequency bandwidth with a slight difference in signal amplitudes. Elsewhere, the discrepancy was significant. This discrepancy was probably attributed to the unresolved unsteady shear layer over the cavity aperture and to numerical dissipation of the shear layer vortices, which are responsible for the pressure tones, frequencies and amplitudes inside the telescope cavity. Also, the CFD-predicted broadband turbulence spectrum was different from the experimental data for unexplained reason.

Using unsteady RANS computations and detached eddy simulation (DES), Schmid *et al.* (2008a), (2008b) and (2009) simulated successfully the flow unsteadiness around and inside the airborne SOFIA telescope (see Fig. 2). For the DES approach, the region across the telescope aperture, where the shear layer spans the cavity opening, was solved using large eddy simulation (LES), as displayed in Fig. 3. Both unsteady Reynolds-averaged Navier-Stokes (URANS) models and DES predicted fairly well all the oscillatory modes and their frequency and amplitude, when compared to experiment. As expected, in general, the results from the DES simulations were in excellent agreement with experimental data. To reduce the sound pressure level inside the telescope cavity, the authors incorporated a few pairs of vortex generators on the front edge of the cavity, which served to thicken and to stabilize the shear layer and thus mitigate the pressure fluctuations inside the cavity. Also, to avoid any acoustic resonance, the authors found that by adding baffles inside the cavity or changing the shape of the cavity, the frequencies of the acoustic modes could be shifted to lower or higher values.
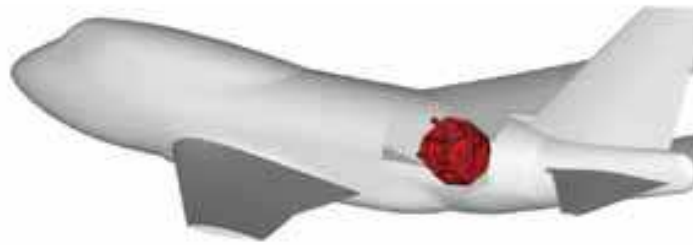
Fig. 2. SOFIA telescope carried on the Boeing 747SP (Schmid *et al*., 2009)

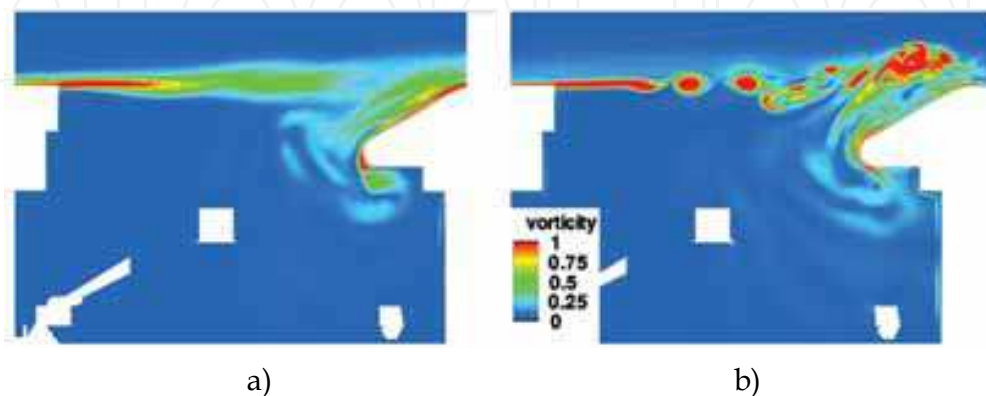| |
|--------|
| a) |
| b) |

Fig. 3. Snapshots of the predicted vorticity patterns across the cavity opening: a) URANS and b) DES (Schmid *et al*., 2009)

Coming back to the ground-based telescope discussion, which represents the main focus of the present chapter, a campaign of scaled-model wind-tunnel measurements and CFD simulations was undertaken at the National Research Council of Canada to estimate wind loads on a very large optical telescope (VLOT) housed within a spherical calotte. The tests were performed for various wind speeds to examine Reynolds number effects, and VLOT orientations, see Cooper *et al*. (2005) and (2004a). The measurements revealed the existence of significant pressure fluctuations inside the enclosure owing to the formation of a shear layer across the enclosure opening. As many as four modal frequencies were detected, depending on the wind speed. The number of modal frequencies decreased with increasing wind speed. The mean pressure inside the enclosure and on the primary mirror surface was roughly uniform. Later on, the effect of the enclosure venting was investigated experimentally by Cooper *et al*. (2004b) by drilling two rows of circular vents around the enclosure. The amplitude of the periodic pressure fluctuations that were measured in Cooper *et al*. (2005) was significantly reduced. The shear layer oscillatory modes were reduced to a single mode with smaller pressure fluctuation amplitude.

In parallel with the aforementioned experimental studies, Mamou *et al*. (2004a-b) and Tahi *et al*. (2005a) numerically investigated the wind loads on a full-scale and scaled model. Comparisons with WT measurements (Cooper *et al*., 2005) showed good agreement for the mean pressure on the enclosure inside and outside surfaces as well on the primary mirror surface. However, some discrepancies between CFD and WT data were observed for the pressure fluctuations and the oscillatory modal frequencies. It was believed that these discrepancies could be attributed to several possible sources. One possible error was the scaling effects, as the CFD solutions were obtained for a full-scale model that corresponded to a Reynolds number that was two orders of magnitude greater than that at the wind tunnel conditions. Second, the viscous effects of the wind tunnel floor were neglected. Since

an inviscid boundary condition was used in the simulations, the horseshoe vortex was not simulated. Third, the flow simulations were run at a relatively higher Mach number (i.e. large time step) to speed up the computations owing to the large grid size of the computational domain. The specification of a high Mach number in the flow simulation has no influence on the compressibility effects. Finally, the freestream flow conditions of Mount Mona Kea used in the CFD simulations were different from those imposed in the wind tunnel.

To understand better the reasons for the differences, Mamou *et al.* (2004c) performed additional CFD simulations based on the scaled model and using the same flow conditions reported in Cooper *et al.* (2005). Non-slip conditions were considered for the floor to account for the formation of a boundary layer that could affect the pressure distribution and the flow field near the enclosure base. Higher simulation Mach numbers and the wind tunnel Mach number were both used. Tahi *et al.* (2005a) also conducted a CFD analysis to predict the wind loading on the primary mirror surface for a 30-m VLOT telescope (an upsized VLOT configuration) with a vented enclosure. The results showed that the pressure fluctuations, when compared to the sealed enclosure configuration, decreased considerably, while the mean pressure on the primary mirror increased. Tahi *et al.* (2005b) also performed detailed and thorough comparisons between CFD predictions and WT measurements for different VLOT configurations and wind conditions. The comparisons were focused mainly on the effect of the pressure wind loads on the primary mirror of the telescope. Grid sensitivity and Mach number effects were reported for a given configuration. It was found that the cause for the discrepancy between CFD and WT data was attributed to the Mach number effect. Using the wind tunnel Mach number, the predicted flow unsteadiness inside the enclosure was in good agreement with the experimental data. Overall, for the approaches, there was a good agreement between the mean pressure coefficients predicted by CFD and those measured on the primary mirror surface.

According to previous CFD simulations studies for flows past ground-based telescopes housed in enclosures, the big challenge is to predict the pressure loads and flow unsteadiness behavior over the primary and secondary mirrors units. As the enclosure opening is subject to unstable shear layer flows, the vortex-structure interactional effects must be well resolved. Unstable shear layers usually lead to the formation of a series of strong vortices (Kelvin–Helmholtz) that are very difficult to simulate or maintain owing to the numerical dissipation effect, which smears the vortices, increases their size and reduces their intensity. To capture well this type of flow behavior, high-order numerical schemes or severe grid refinement is required to reduce the numerical dissipation to an acceptable level. Obviously, grid refinement leads to prohibitive computation times, and the solution becomes impossible to achieve owing to the scale of large telescopes. Also, vortices and structure interaction are a source of acoustic wave generation. These waves are usually three-dimensional and propagate everywhere in the flow domain at the local speed of sound. For cavity flows, there is a mutual interference between aerodynamic and acoustic effects. In other words, acoustic waves affect the shear layer aerodynamics through acoustic excitation, and in turn the shear layer aerodynamics affects the generation of the acoustic waves. Besides these numerical simulation challenges, acoustic waves are also very difficult to maintain and trace owing to their small pressure amplitudes and thickness. Capturing the acoustic waves in the flow domain relies on intensive grid refinement and numerical dissipation mitigation using high-order numerical schemes and relatively small time steps. Obviously, these requirements can render the CFD computations unpractical. The incompressible form of the Navier-Stokes equations is not suitable for cavity free-shear-

layer flow simulations as, besides the inevitable numerical dissipation problem, the acoustic-aerodynamic interaction cannot be addressed.

3. Wind tunnel test

3.1 Model

A 1:100 scale model of the VLOT was tested in the NRC 0.9×0.9 m pilot wind tunnel in the ¾ open-jet configuration (Fig. 4). The tunnel has an air jet 1.0 m wide and 0.8 m high.
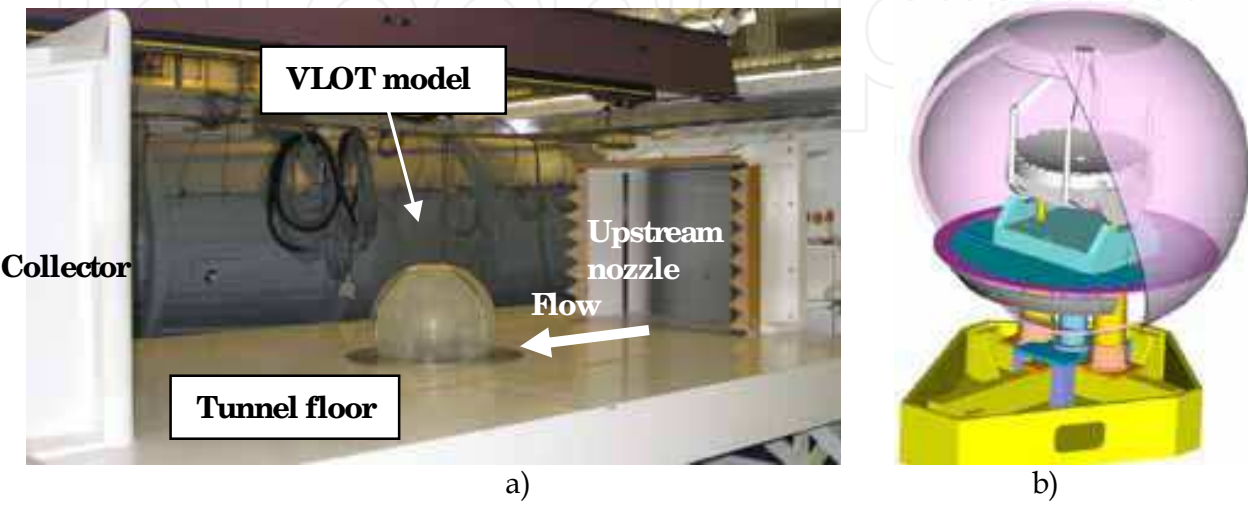

Fig. 4. a) VLOT 1:100 scale model installed in the NRC 0.9×0.9 m open-jet pilot wind tunnel, b) VLOT CAD model and balance assembly (Cooper *et al.*, 2005)

The VLOT model, manufactured using the stereolithography apparatus (SLA) process, included an internal mirror and a spherical enclosure (see Fig. 5). The model external diameter was D = 0.51 m, with a circular opening of 0.24 m diameter at the top of the external enclosure. The measured average roughness height on the VLOT model was 0.13 mm, giving kr/D = 25.5×10^{-5}. The model was mounted on the floor turntable of the test section (see Fig. 4b). The model installation permitted adjustment of the zenith angle ϕ by 15° increments between 0° and 45°, while the floor turntable allowed continuous variations in the azimuth direction $0° \leq \varphi \leq 180°$. The zenith angle $\phi=0°$ corresponds to when the primary mirror is pointing overhead and the azimuth angle $\varphi=0°$ when the mirror is facing the upstream wind at $\phi=90°$.
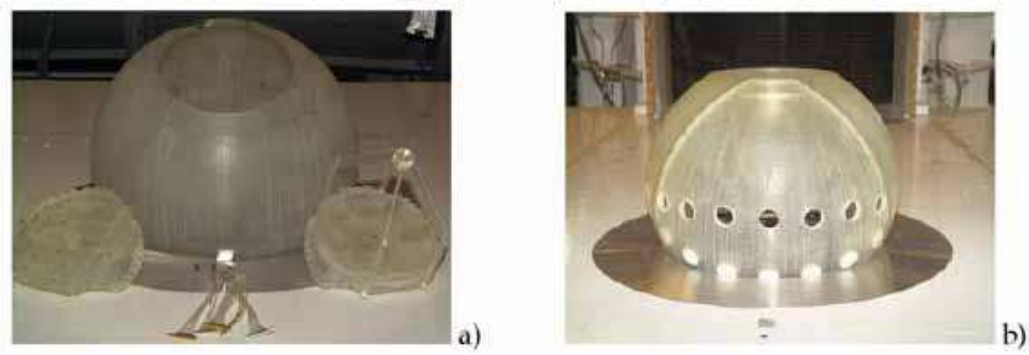

Fig. 5. VLOT wind tunnel model: (a) pressure-instrumented mirror with tubing, enclosure with tubing runs and (b) force mirror assembly (Cooper *et al.*, 2005)

3.2 Wind tunnel flow conditions

The wind tunnel tests were performed under atmospheric flow conditions at various wind speeds and telescope orientations. The wind speed was varied from 10 to 40 m/s, with Reynolds numbers from 3.4×10^5 to 13.6×10^5.

3.3 Unsteady pressure load measurements

As reported in Cooper *et al.* (2005), the enclosure and mirror surfaces were instrumented with pressure taps, as illustrated in Fig. 6. The locations of the pressure taps were described by the azimuth angle, θ, within the enclosure frame. The angle $\theta = 0^\circ$ corresponded to the intersection line between the enclosure and the y-z plane located on the left side of the enclosure when pointing upstream; this line is indicated by column C1 on the enclosure surface (see Fig. 6a). Pressure taps in the enclosure were integrated to the structure. The pressures were scanned at 400 Hz. A few scans were done at 800 Hz to show that no additional frequency content was present above 200 Hz. The dynamic response of each pressure tube was calibrated up to 200 Hz using a white noise signal source. The resulting transfer function of each tube was used to correct for the dynamic delay and distortion resulting from the tubing response.
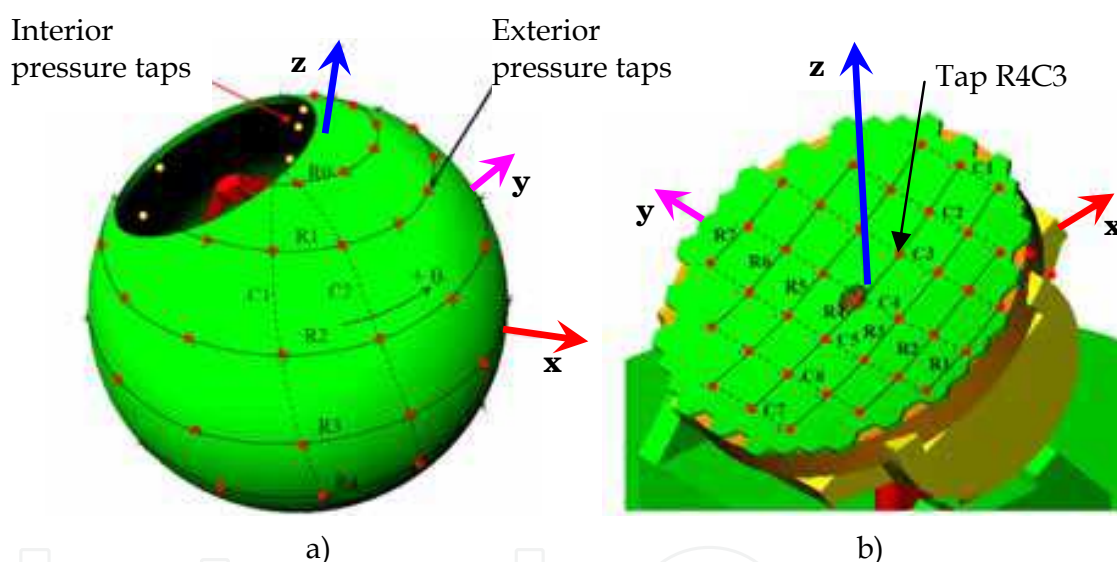

Fig. 6. Pressure taps on: (a) the exterior and interior enclosure surfaces, and (b) the primary mirror surface (Mamou *et al.*, 2008)

3.4 Infrared measurements

In parallel to the pressure load measurements, infrared (IR) measurements were conducted to determine the location of the transition between laminar and turbulent flow, as well as to determine the separation location on the spherical model enclosure. The Agema Thermovision 900 infrared camera used for this test had an image resolution of 136×272 pixels covering a field of view of roughly 10×20°. The camera operated in the far infrared 8–12 μm wavelength and could acquire four frames per second. To improve the data quality, 16 consecutive images were averaged and stored on disk. The camera sensitivity and accuracy were 0.08°C and ±1°C, respectively. The model emissivity was $\varepsilon = 0.90$. For all the test runs, the camera was positioned on the left-hand side of the test section (when facing the flow), providing an excellent side view of the model.

3.4.1 Principles of IR measurements

The transition detection using IR was based on the difference in convective heat transfer between the air flow and the model skin. The heat transfer is basically affected by the nature of the boundary layer. Compared with laminar flow, the heat transfer is significantly greater in the turbulent flow regime. The different levels of heat transfer become visible when the model and air temperatures are different.

In practical wind tunnel applications, artificial temperature differences between the air flow and the model can be introduced by controlling the air temperature, Mébarki (2004) and Mébarki *et al*. (2009). Two methods were used in the present study to enhance the heat transfer between the model and the air flow.

For wind speeds below 30 m/s, the tunnel was operated first at maximum speed to heat the model. Then the wind speed was reduced to the target speed and the air temperature was reduced by turning on the wind tunnel heat exchanger. During this cooling process, several images were acquired and recorded for later analysis.

For the maximum speed of 40 m/s, the tunnel heat exchanger was unable to absorb the substantial heat generated by the tunnel fan. In this case, the model was first cooled using low speed flow (~10 m/s) with the heat exchanger operating, and then the tunnel heat exchanger was turned off and the air speed was set to the maximum target speed. After a moment, the air started to heat the model.

3.4.2 Heat transfer computation

The convective heat transfer coefficient was estimated from the sequence of temperature images recorded during the cooling or heating processes using a one-dimensional analysis of heat transfer inside a semi-infinite medium and neglecting the heat transfer with the surrounding medium due to radiation. The objective of this computation was not to obtain accurate heat transfer data, but to gain information about relative changes of the heat transfer coefficient at the surface of the model, and therefore better identify the various flow regimes (laminar, turbulent and separation). The method of Babinsky and Edwards (1996), used here, involved the resolution of the convolution product of the surface temperature changes and time. This equation was solved in Fourier space using the convolution theorem

$$h(T - T_r) = \frac{1}{2}\sqrt{\frac{\rho\,c\,k}{\pi}} \int_0^t F(T)G(t)d\tau \tag{1}$$

with $F(T) = T - T_0$ and $G(t) = (t - \tau)^{-1/2}$.

In Eq. (2), t is the time, h is the convective heat transfer coefficient, T_0 and T are the initial ($t = 0$) and current (time t) model temperatures, T_r is the adiabatic wall temperature of the flow computed with a recovery factor $r = 0.89$, and β is the thermal product given by $\beta = (\rho c k)^{1/2}$, where ρ is the density, c is the specific heat and k is the thermal conductivity of the medium. In the present evaluation, the thermal characteristics of Plexiglas were used to approximate the model characteristics ($\beta = 570$).

From the heat transfer coefficient, the Stanton number was computed as follows:

$$St = \frac{h}{\rho_{air}\,Cp\,V} \tag{2}$$

where St is the Stanton number, and ρ, Cp and V are respectively the air density, specific heat at constant pressure, and velocity. Since the objective of this computation was to obtain sufficient resolution between the various flow regimes rather than accurate heat transfer data, the resulting Stanton numbers were normalized by a reference value. This reference value was based on the correlation from White (1983), giving an expression for an average Nusselt number for a sphere:

$$Nu_0 = 2 + Pr^{0.4}(0.4Re^{0.5} + 0.06Re^{2/3}) \qquad (3)$$

where Nu is the Nusselt number, Pr is the Prandtl number (Pr = 0.7 for air) and Re is the Reynolds number based on the model diameter. The reference Stanton number was obtained using:

$$St_0 = Nu_0 / RePr \qquad (4)$$

4. Computational fluid dynamics

4.1 VLOT CAD model

The CAD geometry of the VLOT wind tunnel model shown in Fig. 6 was used in the CFD simulations without any simplification. According to a study of flows past a rough sphere by Achenbach (1974), there is no significant difference in the drag coefficient of a sphere in smooth flow at a low supercritical Reynolds number over the range $0 \leq kr/D \leq 25 \times 10^{-5}$. For the current model surface roughness very close to $kr/D = 25 \times 10^{-5}$, it appears that at the test Reynolds number of Re = 4.6×10^5 and with low wind tunnel turbulence intensity of 0.5%, the flow is likely supercritical. Within this range $0 \leq kr/D \leq 25 \times 10^{-5}$, the mean flow conditions remain similar to those for a smooth surface. The computational domain was delineated by the model surface, wind tunnel floor and a farfield that was located 15D upstream of the enclosure, 18D downstream of the enclosure, 14D away from the sides of the enclosure, and 30D above the enclosure. Since the flow was nearly incompressible, the location of the farfield boundaries at these distances was assumed to be appropriate for the computations, and the effect of the domain boundaries on the solution was expected to be negligible. This facilitated comparisons with the WT measurements, which were corrected for blockage effect.

The freestream flow conditions used in the current simulations matched those measured in the wind tunnel, however a higher Mach number was used in three simulations. The wind tunnel floor was located at an elevation 0.125 m below the pivot telescope axis. The position of the upstream edge of the viscous floor boundary layer was calculated using a measured velocity profile at some distance upstream from the model center and applying a turbulent boundary layer approximation (McCormick, 1979). To minimize the grid size within the flow field, viscous conditions were applied only to a small region of the floor around the telescope enclosure. The upstream and downstream edges of the viscous region were fixed at 5.46D and 1.75D from the model position, respectively. The viscous region extended 0.9D from the sides of the model.

4.2 Grid topology and flow solver

After defining the VLOT CAD model and the farfield, the flow domain was discretized into cubic elements called voxels. As displayed in Fig. 7, to optimize the number of voxels used

in the simulations, seven levels of variable resolution (VR) regions were created to adequately distribute the voxels according to the pertinence of the flow details around and inside the VLOT enclosure. Five levels of VR regions were created outside the enclosure and two VR region levels were created inside the enclosure. In each VR region, the grid remained Cartesian and uniform. The voxel edge length was multiplied or divided by a factor of two across the VR region interfaces. To predict accurately the pressure drag and the separation line, the grid was refined on the back of the enclosure around the telescope structure and along the observation path, as shown in Fig. 7. The grid resolution within the highest-level VR region was set to 1.1 mm.

The grid size of the entire flow domain was about 26.7 million voxels. To speed up the computations, the CFD simulations were performed in two steps. First, the solution was marched in time on a coarse mesh (about 11 million voxels), for about 100k time steps, in order to dampen rapidly the transient effects. The solution was initiated with uniform flow in the computational domain and with the stagnation condition inside the enclosure. Then, the resulting solution was mapped over to the refined mesh using linear interpolations. Then, the computations were performed until the unsteady behavior of the aerodynamic forces reached a periodic or aperiodic state.
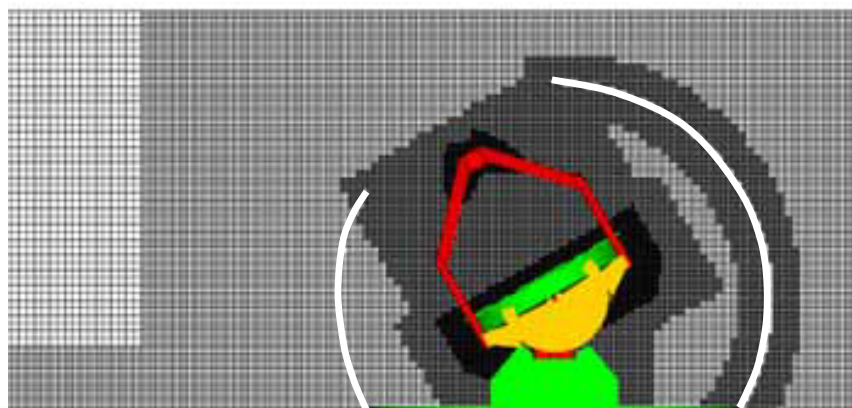

Fig. 7. Voxel distribution on a plane cutting through the telescope configuration ($\phi = 30^{\circ}$ and $\varphi = 0^{\circ}$). The enclosure cross-section is displayed in white (Mamou *et al.*, 2008)

4.3 Modelling of flow separation and boundary layer transition
4.3.1 Modelling of flow separation
The CFD simulations were performed using the time-dependent CFD PowerFLOW™ solver. The solver uses a lattice-based approach, which is an extension of the lattice-gas/Boltzmann method (LBM). The LBM algorithm is inherently stable and with low numerical dissipation, which is suitable for acoustic wave simulation. For high Reynolds number flows, turbulence effects are modeled using the very large eddy simulation (VLES) approach based on the renormalization group theory (RNG) form of the k-ε turbulence model. It resolves the very large eddies directly (anisotropic scales of turbulence) and models the universal scales of turbulence in the dissipative and inertial ranges. The code contains wall treatments equivalent to the logarithmic law-of-the-wall with appropriate wall boundary conditions. The effects of adverse pressure gradients are simulated by modifying the local skin friction coefficient, which allows an accurate prediction of the flow separation location. The effect of the sub-grid scale turbulence is incorporated into the LBM through the eddy viscosity.

4.3.2 Modelling of flow transition

When three-dimensional transition occurs over non-slip surfaces and/or in free shear layers, the flow behavior is far away from being addressed by current commercial CFD codes. To resolve such complex flows, hybrid CFD techniques are required. Such techniques may involve DNS, LES and URANS simulations at the same time. DNS can be applied to a small region around the edge of the opening to track the evolution of the Tollmien–Schlichting (TS) waves, and further LES can be used to track the Kelvin-Helmholtz (KH) waves and reproduce the interactional flow mechanism as the shear layer impinges on the aft edge of the opening. In the present CFD work, the flow simulations were fully turbulent as the code does not allow for transition. Owing to the complex external flow behavior around the sphere-like enclosure, this was not a good approximation in the critical-supercritical range where the wind tunnel tests were performed. According to the discussion of Section 4.1, the assumption of fully-turbulent flow might be acceptable at the experimental Reynolds number; however, further validation simulations are desirable to assess the effect of transition occurring on an appreciable distance from stagnation. The intent of the IR investigation was to produce for future CFD code validation some experimental data concerning the transition and separation locations on the telescope configuration. However, as discussed below, the flow behavior around a base-truncated-spherical enclosure with an opening at various orientations can be quite different from that reported by Achenbach (1974) for an isolated sphere. However, from the good comparison between CFD and experimental results for the mean pressure loads on the enclosure surface and the pressure fluctuations inside the enclosure, it appears that the flow inside the enclosure was not significantly affected by the transitional and separated flow regions on the enclosure surface. Thus, running the flow simulation with fully turbulent conditions over a smooth surface was believed to be a fair assumption.

5. Results and discussion

In the present chapter, some CFD and experimental data are discussed for a specific configuration. Owing to the limited budget of the project and the high cost of the CFD simulations, only a few telescope configurations were performed.

5.1 Infrared measurement data

The intent of the infrared measurements was to visualize the boundary layer flow behavior on the external surface of the telescope enclosure, distinguishing between laminar and turbulent flows, and attached and separated flows, which could be useful for future CFD code validations.

Figure 8 shows examples of raw images obtained at a speed of $V = 10$ m/s for the model configuration $\phi = 30°$ and $\varphi = 0°$. At this speed, a temperature variation of 2°C to 3°C was visible, separating the laminar boundary layer from the turbulent boundary layer on the model. The image processing was performed to extract quantitative information from the IR data. Of particular interest was the location of transition and the separated flow regions at the rear of the model. For this purpose, a bi-cubic polynomial transformation was used to convert the IR image coordinate system into the model spherical coordinate system using control points on the VLOT model, with an accuracy of 1° RMS for both the zenith (ϕ) and azimuth (φ) angles, estimated using the pressure taps on the model.
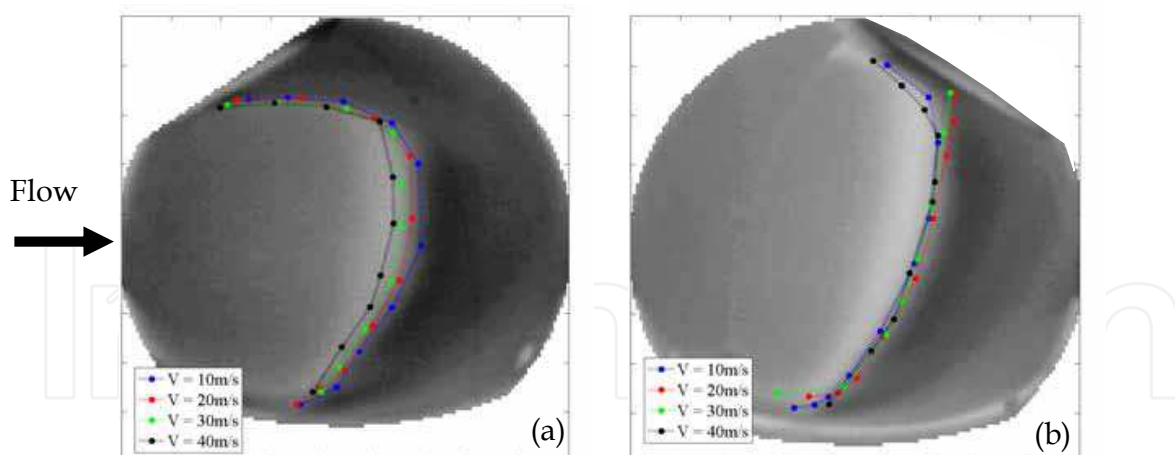
Fig. 8. Effect of wind speed on the transition locations (dotted lines) overlaid over the temperature image obtained at V = 10 m/s for two configurations: (a) model at ϕ = 30° and φ = 0°, (b) model at ϕ =30° at φ =180°

The IR results shown in Fig. 8 were obtained for various speeds and model azimuth positions: (a) φ = 0° and (b) φ = 180°. The transition locations were extracted from the temperature images and overlaid on top of the IR images recorded at V = 10 m/s.

The effect of the opening on the transition location is visible when comparing the two model orientations shown in Fig. 8a and b. In the case of an azimuth of 0°, the maximum transition location, starting at θ = 15° near the centerline on the model for the minimum speed, moved forward with increasing speed by about 2.5° per 10 m/s increment (Fig. 8a). The shape of the transition line was also curved towards the front of the telescope near the external envelope opening. The laminar flow did not extend past the opening, which triggered the turbulence at an azimuth of 0°.

On the other hand, the opening did not affect the transition location much in the case of an azimuth of 180°, as shown in Fig. 8b. In this case, the maximum transition location on the model, about θ = 205°, appeared fairly insensitive to the Reynolds number, except in the vicinity of the opening. The resulting normalized Stanton number (St/St_0) distributions are given in Fig. 9 for model azimuth positions of 0° and 180°, with the levels indicated, unlike the raw temperature images shown in Fig. 8. From the Stanton number distributions in Fig. 9, the estimated transition and separation lines were not sensitive to the test procedure (*e.g.*, model cooling or heating).

The estimated transition lines and separation lines at the rear of the VLOT model are shown on the images. The heat transfer coefficient (and, therefore, *St*) increased suddenly as the boundary layer transitioned from laminar to turbulent. Then, as the turbulent boundary layer thickened, the skin friction was reduced and the heat transfer coefficient decreased again. In contrast, the flow separation induced a nearly constant heat transfer coefficient in the reversing flow region. Therefore, the separation region was estimated from examination of the constant Stanton number regions at the rear of the model. The attached flow extended to a maximum of about θ = 30° for φ = 0° and θ = 210° for φ = 180° on the model. At V = 10 m/s, as displayed in Fig. 9, the estimated transition and separation lines for φ = 0° and φ = 180° agreed quite well with the flow visualization performed using mini-tufts on the model's surface (Cooper *et al.*, 2005), although the mini-tufts affected the surface flow behavior locally.

From the IR measurements, for the φ = 0° case over the range of wind speeds tested, the boundary layer separated in its laminar state right at the front edge of the opening. The flow

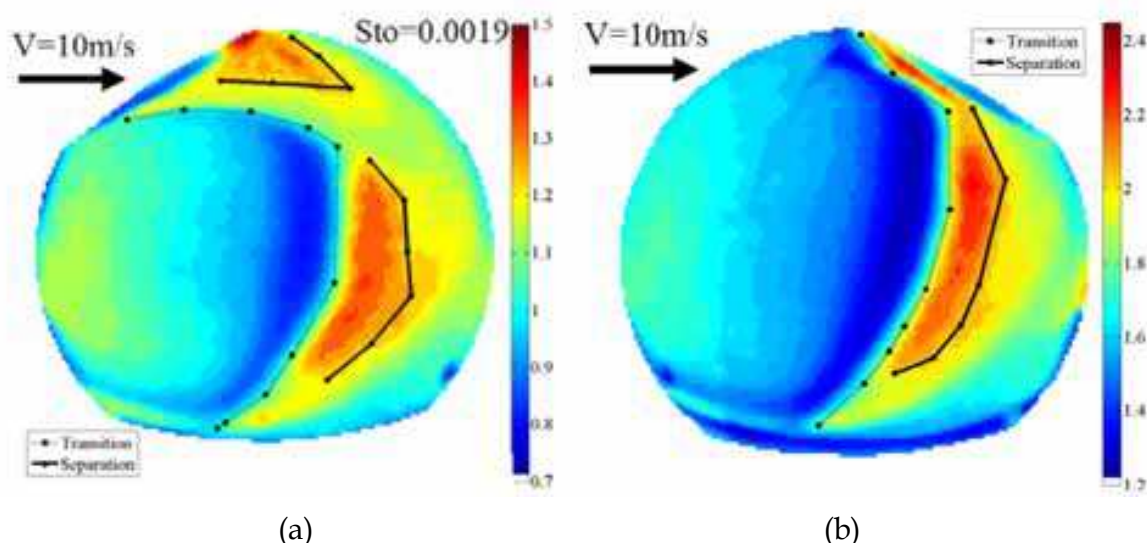(a)   (b)

Fig. 9. Stanton number (St/St_0) distribution and estimated transition and separation lines for a) $\varphi = 0°$ and b) $\varphi = 180°$ azimuth angles

on the sides of the opening seemed to experience transition to turbulence at about mid-diameter of the opening. Beyond the aft edge of the opening, the flow appeared to be turbulent. These experimental observations reveal that the free shear layer underwent transition from the laminar to turbulent state before reaching the aft edge of the opening. The transition line might be three dimensional owing to the circular shape of the opening. Then the shear layer, before reaching the front edge to the transition location, might contain unstable TS waves that were transported into the main stream. A bit further downstream, a combination of TS and KH waves could coexist and interact, leading to a much more complex unsteady flow over the enclosure opening.

5.2 Unsteady wind loading measurement data

During the wind tunnel tests performed by Cooper *et al*. (2005) and (2004a-b), various wind speeds and telescope orientations were considered. When the enclosure opening was directly pointing into the wind ($\varphi = 0°$ with $0° \leq \phi \leq 30°$), strong pressure fluctuations were present in the enclosure, displaying one to four periodic oscillatory modes, which were mainly caused by the oscillatory nature of the shear layer forming over the enclosure opening (see Fig. 10). The number of modes decreased as the wind speed increased, which corresponded to a notable increase in the peak power-spectral-density of the pressure signal. The pressure fluctuations became significant when the Helmholtz cavity mode was excited, when all the pressure taps inside the model were excited by an almost identical unsteady pressure loading. The mean pressure inside the enclosure was almost uniform and had the magnitude of the pressure distribution of the external pressure field at the enclosure opening. It was observed that, when increasing the speed from 10 to 41 m/s, the enclosure resonance was first exited by the fourth mode, followed at higher speeds by successively lower modes. However, the first and second modes resulted in the largest pressure fluctuation amplitude inside the enclosure, as these two modes excited the enclosure at the Helmholtz frequencies. According to the averaged measurements of the interior pressure taps, the mirror surface had a pressure field almost identical to that on the enclosure interior surface. The mean and rms pressure distributions over the inner surface of the enclosure

were nearly uniform, with little or no significant phase difference observed over the mirror surface. For a vented enclosure, as seen in Fig. 10, only one oscillatory mode appeared, with its frequency slightly reduced by the ventilation effect. This indicated a weaker interaction of the shear layer with the enclosure opening edge. To illustrate the flow patterns past the telescope enclosure, smoke visualization was applied around and inside the enclosure, showing that the flow was massively separated on the back of the enclosure, while a strong horseshoe vortex was formed on the floor around the front part of the enclosure.
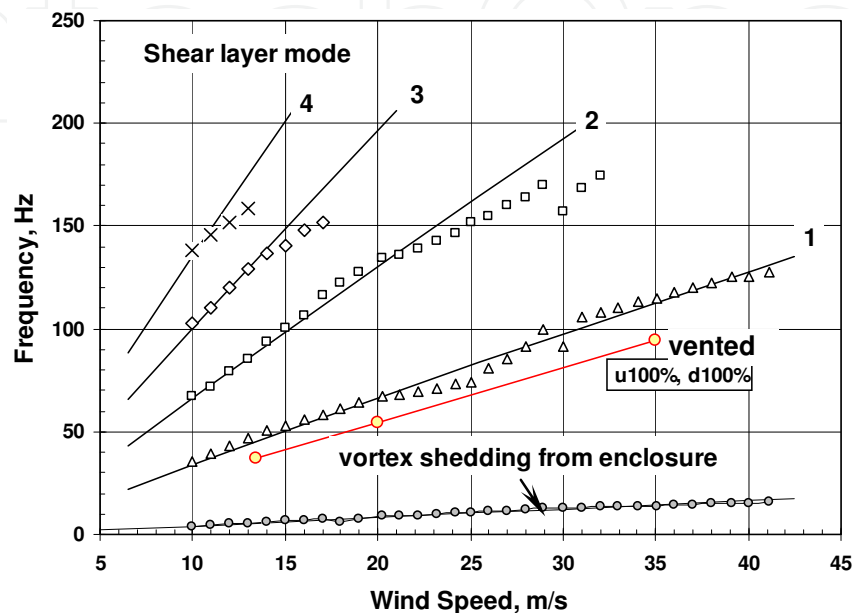
Fig. 10. Cavity oscillation behavior at $\phi = 0^\circ$ and $\varphi = 0^\circ$ for a sealed enclosure (black curves and symbols) and a vented enclosure (red curve and symbols) (Cooper *et al.*, 2004b)

5.3 CFD results compared to experimental data

For the purpose of the CFD analysis, this section focuses on the results obtained from both wind tunnel measurements and CFD simulations at one wind speed (13.4 m/s) and four azimuthal and two zenithal orientations. In general, both experimental and CFD investigations revealed unsteady flows past the telescope structure for all orientations. The results are presented in terms of the time history of the forces, pressure coefficients, and flow patterns. For comparisons with experimental data (Cooper *et al.*, 2005), mean values of the pressure coefficients and their standard deviations were computed at the pressure tap locations on the outer and inner surfaces of the enclosure, as well as on the primary mirror surface. A spectral analysis was also performed for the pressure coefficient signal collected at one (R4C3) of the pressure taps on the primary mirror surface. Grid sensitivity and time-step size refinement effects were investigated.

In the PowerFLOW™ solver, the time-step value is defined implicitly by specifying the finest voxel size, the maximum velocity, and the simulation Mach number. To speed up the computation, the simulation Mach number (*i.e.*, Ma = 0.228) was chosen to be greater than the physical Mach number (Ma = 0.0391). After solution convergence, two or three of the periodic cycles were simulated, from which statistical quantities were estimated. The simulation time step was $\Delta t = 22.23$ μs for the coarse mesh and $\Delta t = 14.82$ μs for the fine mesh. The coarse mesh solution was marched for 2.40 s of simulated time, and then the refined mesh solution was computed for an additional 1.596 s of simulated time.

5.3.1 Flow patterns

Snapshots of detailed flow patterns are illustrated in Fig. 11. On the back of the telescope enclosure, the flow was separated and several vortices were formed. Flow separation also took place at the aft edge of the opening, from which periodic vortices emanated and were shed downstream. Since a boundary layer formed on the non-slip floor a horseshoe vortex was formed and its core was clearly visible on the floor ahead of the enclosure base, as shown in Fig. 11. Over the opening, the flow was complex, where it sometimes entered the enclosure through a small area near the aft edge of the opening and spilled out from both sides of the opening. Snapshots of the vorticity magnitude field for various telescope orientations are shown in Fig. 11(a-c), when the opening was facing into the wind, and a snapshot of the static pressure field is displayed in Fig. 11d, when the opening was facing downstream. In all cases, the vorticity-time histories showed that a strong free shear layer formed across the opening, starting from the upstream edge of the opening and extending towards the aft edge. The free shear layer developed into a series of vortices that sometimes impinged on the downstream edge, leading to instantaneous changes in the pressure field inside the enclosure, and sometimes passed over the edge or entered the enclosure. When the enclosure was facing downstream, Fig. 11d, the opening was totally submerged within the separated flow region, accompanied by low pressure fluctuations inside the enclosure.

a) $\phi = 0^{\circ}$ and $\varphi = 0^{\circ}$ b) $\phi = 30^{\circ}$ and $\varphi = 0^{\circ}$

c) $\phi = 30^{\circ}$ and $\varphi = 30^{\circ}$ d) $\phi = 30^{\circ}$ and $\varphi = 180^{\circ}$
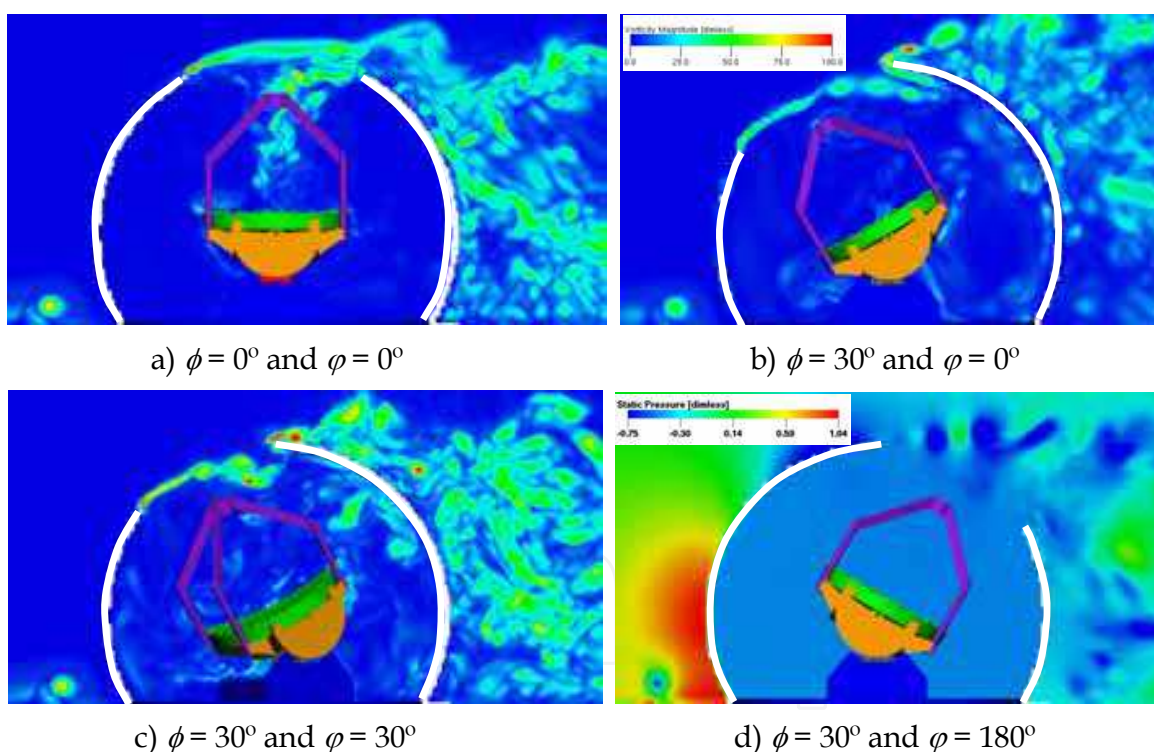
Fig. 11. Time snapshots of flow patterns colored by the vorticity magnitude (a, b and c) and the static pressure magnitude (d) on a centerline plane (Mamou *et al.*, 2004a, 2008)

Snapshot of the off-body streamlines past the enclosure shown in Fig. 12a indicates that the air stream across the opening was intermittently deflected inside and outside the enclosure, owing to the unstable shear layer that formed across the opening. A primary unsteady horseshoe vortex followed by a secondary vortex formed on the floor below the stagnation region on the enclosure. The results showed that the secondary vortex periodically grew and

decayed in size, causing the primary vortex to move slowly back and forth on the floor (time evolution not shown here). The iso-surface of the vorticity magnitude, illustrated in Fig. 12b, showed that the flow past the enclosure opening and in the wake region displayed very complex patterns. Iso-surfaces colored with the actual pressure values clearly illustrated the shape of the horseshoe vortex formed on the floor and the shape of the vortices formed along the shear layer over the enclosure opening. The vortices shed at the aft edge of the opening were also quite visible.
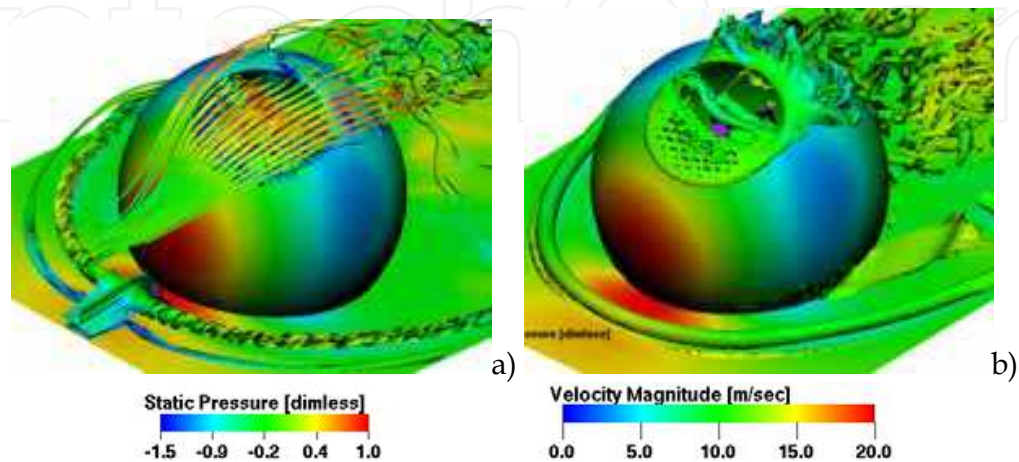
Fig. 12. a) Surface pressure and off-body streamlines colored by the velocity magnitude, b) surface pressure and vorticity iso-surfaces over the floor and the enclosure opening, colored by the static pressure field ($\phi = 30^\circ$ and $\varphi = 30^\circ$) (Mamou *et al.*, 2004a, 2008)

For a qualitative comparison between CFD predictions and experimental observations, a smoke stream was used in the wind tunnel to visualize the flow behavior around the enclosure structure. Figure 13a displays the smoke stream close to the enclosure opening when it was facing the wind ($\phi = 30^\circ$ and $\theta = 0^\circ$), showing a massive flow separation right
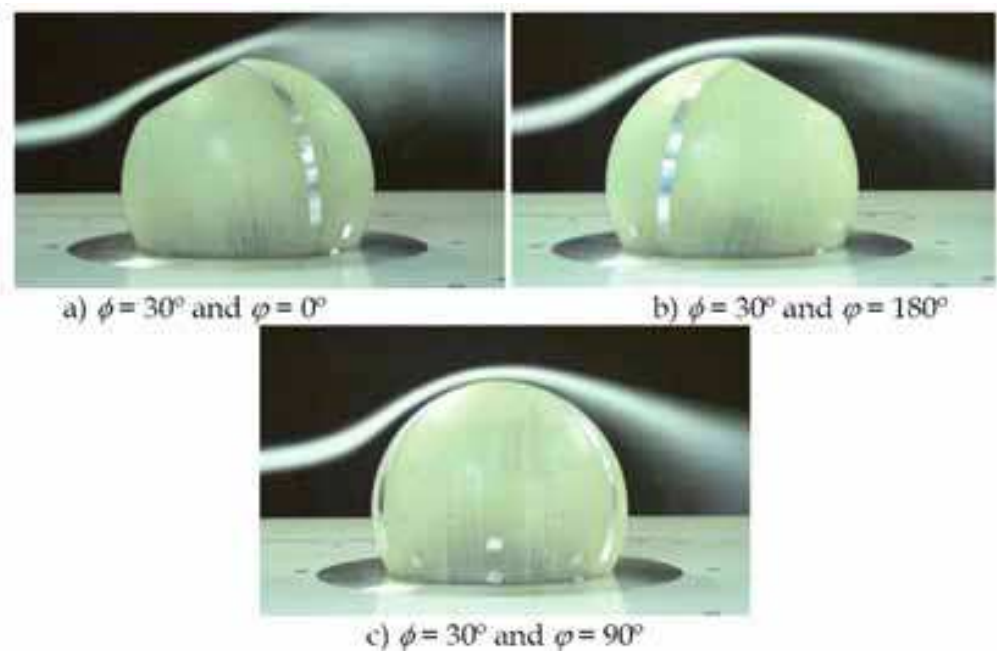
Fig. 13. Smoke stream close to the opening at $V = 13.4$ m/s (Cooper *et al.*, 2005)

after the aft edge of the opening. Figure 13b illustrates the smoke stream when the opening was facing downstream (ϕ = 30º and θ = 180º). It is clear that the enclosure opening was located within the separated flow region, in agreement with the CFD predictions in Fig. 12d. The flow behavior around the sphere-like enclosure was different from that of free sphere flow in the supercritical regime, Achenbach (1974). This is clearly visible in Fig. 13a-b, when the enclosure opening is facing upstream and downstream. The enclosure opening, combined with the floor effect, as shown by the infrared measurements (Fig. 8), had a significant effect on the loci of the separation and transition locations, which were different from those observed on a plain sphere under the same flow conditions. Nevertheless, Fig. 13c suggests that for φ = 90º, the flow separated near θ = 120º measured from the stagnation point, consistent with the assumption of supercritical flow (see Section 4.1).

5.3.2 Telescope aerodynamic forces

To describe the flow unsteadiness behavior and to examine the CFD solution convergence, the time history of the telescope force coefficients (lift and drag) are presented in Fig. 14 for ϕ = 30º and φ = 30º. The CFD results were obtained using the simulation Mach number. The mesh refinement had a negligible effect on the accuracy of the force history. The forces acting on the telescope were close to zero mean value, but exhibited relatively large fluctuations.
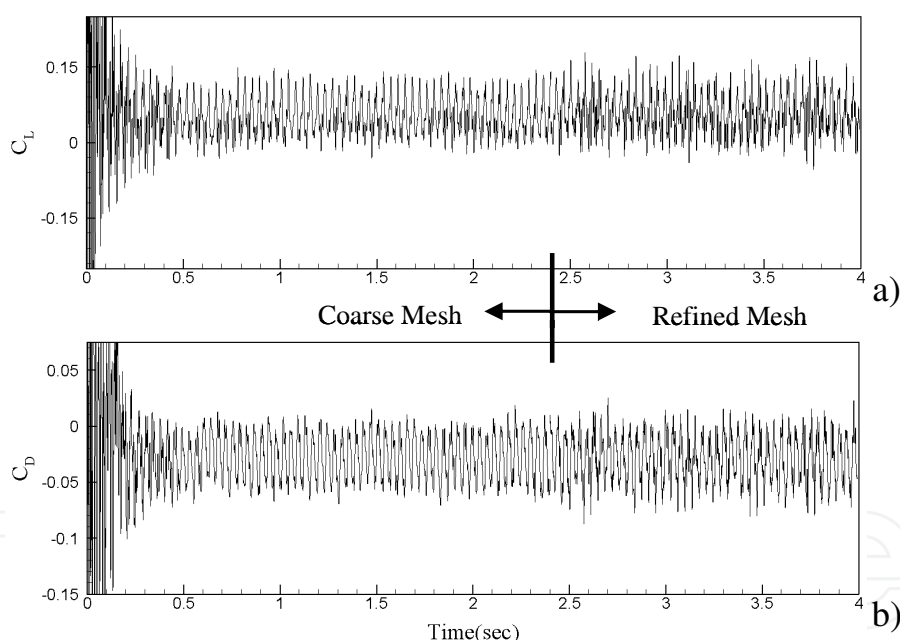

Fig. 14. CFD lift and drag force coefficients on the primary mirror assembly (ϕ = 30º and φ = 30º) (Mamou *et al.*, 2008)

5.3.3 Pressure signal and spectral analysis

The results discussed here were obtained for the ϕ = 30º and φ = 30º configuration. From the CFD simulations and experimental measurements, the pressure signals collected on the primary mirror showed that the mirror surface was excited by roughly the same pressure tones. Hence, only the signal collected at pressure tap R4C3 (see Fig. 6b) is presented. Figure 15 displays the CFD predicted pressure coefficient time history compared to the

measured signal, which was filtered at 400 Hz. The CFD results were obtained using the real Mach number, which allowed capturing of the interactional effects between the shear layer and the generated acoustic waves. As can be seen from Fig. 15, the trend and the amplitude agreed very well, even though the CFD signal contained an additional low energy, high frequency component.
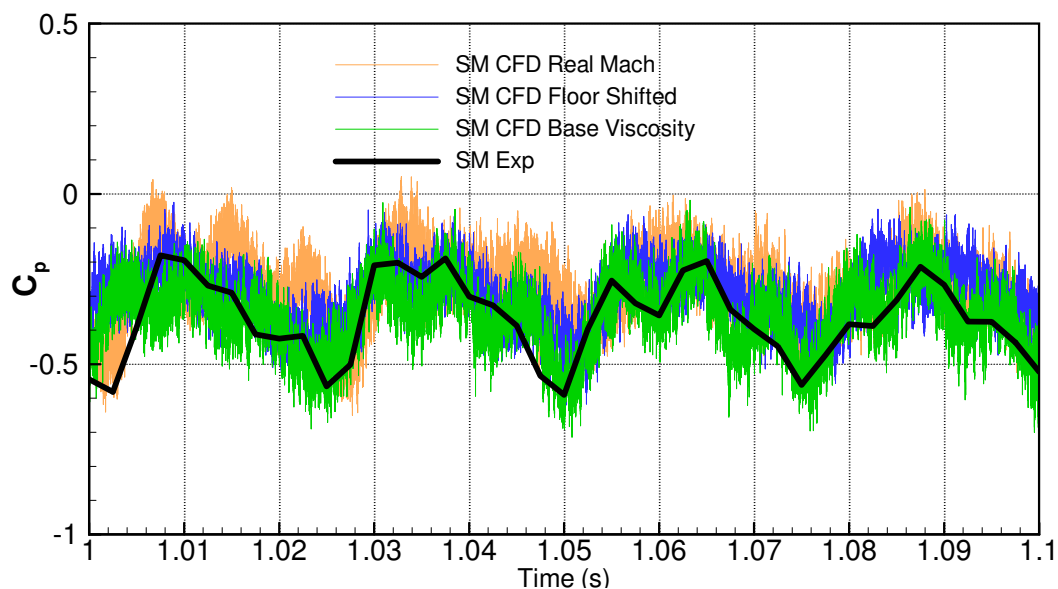

Fig. 15. Instantaneous CFD and experimental pressure coefficients collected on one of the mirror probes, R4C3 ($\phi = 30°$ and $\varphi = 30°$).

As shown in Fig. 16, the power spectral density of the pressure signal on the primary mirror showed a noticeable discrepancy between the CFD simulation Mach number results and the measured data. As discussed in the introduction, a number of flow simulations were performed to investigate how to resolve better the flow past the telescope and obtain a good comparison between the CFD and experimental results. Since further grid refinement did not improve the comparison (Mamou *et al.*, 2008; Tahi *et al.*, 2005), attention was turned to the flow solver time step definition. In the PowerFLOW™ solver, the time step size was computed using the following formula:

$$\Delta t = 0.794 \, Ma \frac{\Delta l}{V_\infty} \tag{5}$$

where *Ma* is the Mach number and $\Delta l = 1.1$ mm is the size of the finest voxel in the computational domain. The simulation Mach number used in PowerFLOW™ was approximately *Ma* = 0.228, such that the virtual-physical time step was maximized to accelerate convergence. This was done intentionally, as it was not expected that the acoustic effects on the flow around and inside the telescope enclosure were significant. To examine the Mach number effect on the flow unsteadiness, a flow solution was obtained using the wind tunnel Mach number *Ma* = 0.039 (real Mach number; denoted by "SM CFD Real Mach" in Fig. 15), which resulted in a smaller time step. The solution was marched for a period of 0.75 s of simulated time, starting with uniform flow outside the enclosure and a stagnation condition inside the enclosure. As expected, the simulation at the wind tunnel Mach number considerably improved the prediction of the power spectral density functions,

as shown in Fig. 16. The new results were in excellent agreement with the wind tunnel measurements obtained for the three modal frequencies. The oscillatory flow behavior over the enclosure opening and inside the enclosure was dominated mainly by the acoustic effects resulting from the interaction of the shear layer with the aft edge of the enclosure opening. When the flow solutions were computed using a Mach number greater than the physical value, the interaction between the opening shear layer and the acoustic waves that existed in the flow was severely affected.

For the simulation at the experimental Mach number, some grid adjustments were needed to improve the CFD results (pressure histories as displayed in Fig. 15), as the turbulent eddy viscosity was overestimated on the digital tunnel floor, which cut through the voxels. A simulation was run by shifting the tunnel floor up to match a complete voxel edge, and referred to as "SM CFD Floor Shifted". The results, obtained for this case, gave a better mean C_P with no change to the frequency domain of the pressure signal, nor to its rms value. Another simulation run by setting a threshold for the base viscosity, denoted by "SM CFD Base Viscosity", agreed much better with the experiment in terms of the pressure signal.
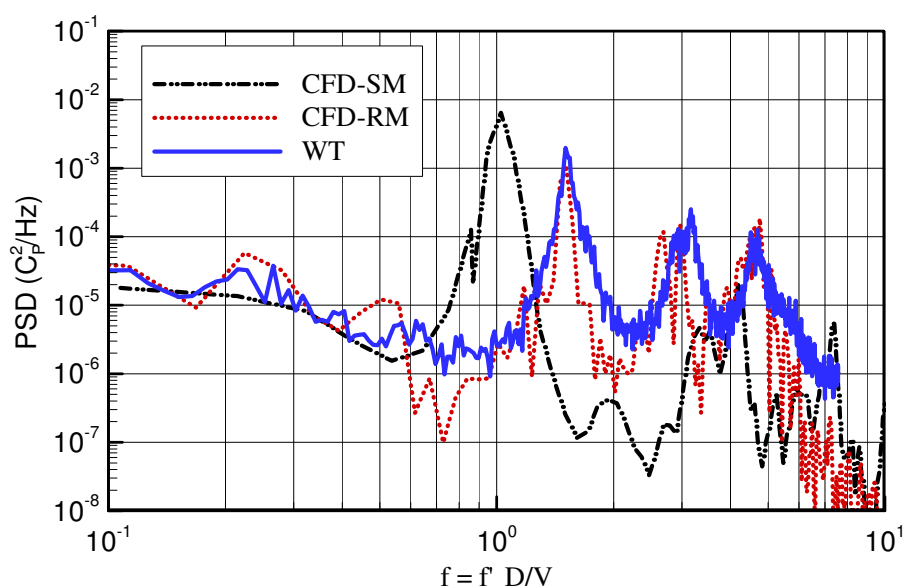

Fig. 16. CFD and experimental power density spectra pressure coefficients collected on one of the mirror probes, R4C3 ($\phi = 30°$ and $\varphi = 30°$) (Mamou et al., 2008)

5.3.3 Mean and standard deviation of the pressure coefficients

The CFD mean pressure coefficients and their standard deviations for pressure tap Row 2 around the outer and the inner surfaces of the enclosure and on the primary mirror surface are compared to the measurements in Fig. 17. The plots on the left side show the C_{Pm} values and the plots on the right side show the standard deviations. The CFD results obtained at the simulation Mach number are referred to as "CFD-SM" and the results obtained at the real Mach number are referred to as "CFD-RM". Overall, the mean pressure coefficients, Figs 17a, b and c, along Row 2 on the enclosure exterior and interior surface and on the primary mirror surface, respectively, showed a good agreement between the CFD predictions and measurements. According to the pressure plateau in Fig. 17a, the flow separation area on the back of the enclosure occurred within the range $0 \lesssim \theta \lesssim 100°$. For a quantitative comparison, the measured pressure coefficient uncertainty at a wind speed of

13.4 m/s was ±0.006. In Fig. 17, the uncertainty is represented by the height of the square symbols. Furthermore, good agreement was observed between the CFD and measured rms C_P data displayed on the right side of Fig. 17, with some slight discrepancies close to the separated region. Inside the enclosure, the C_{Pm} plots in Fig. 17b and c indicated that the mean pressure was almost uniform inside the enclosure. The amplitude of the CFD-predicted pressure fluctuations was higher than that of the wind tunnel measurements.
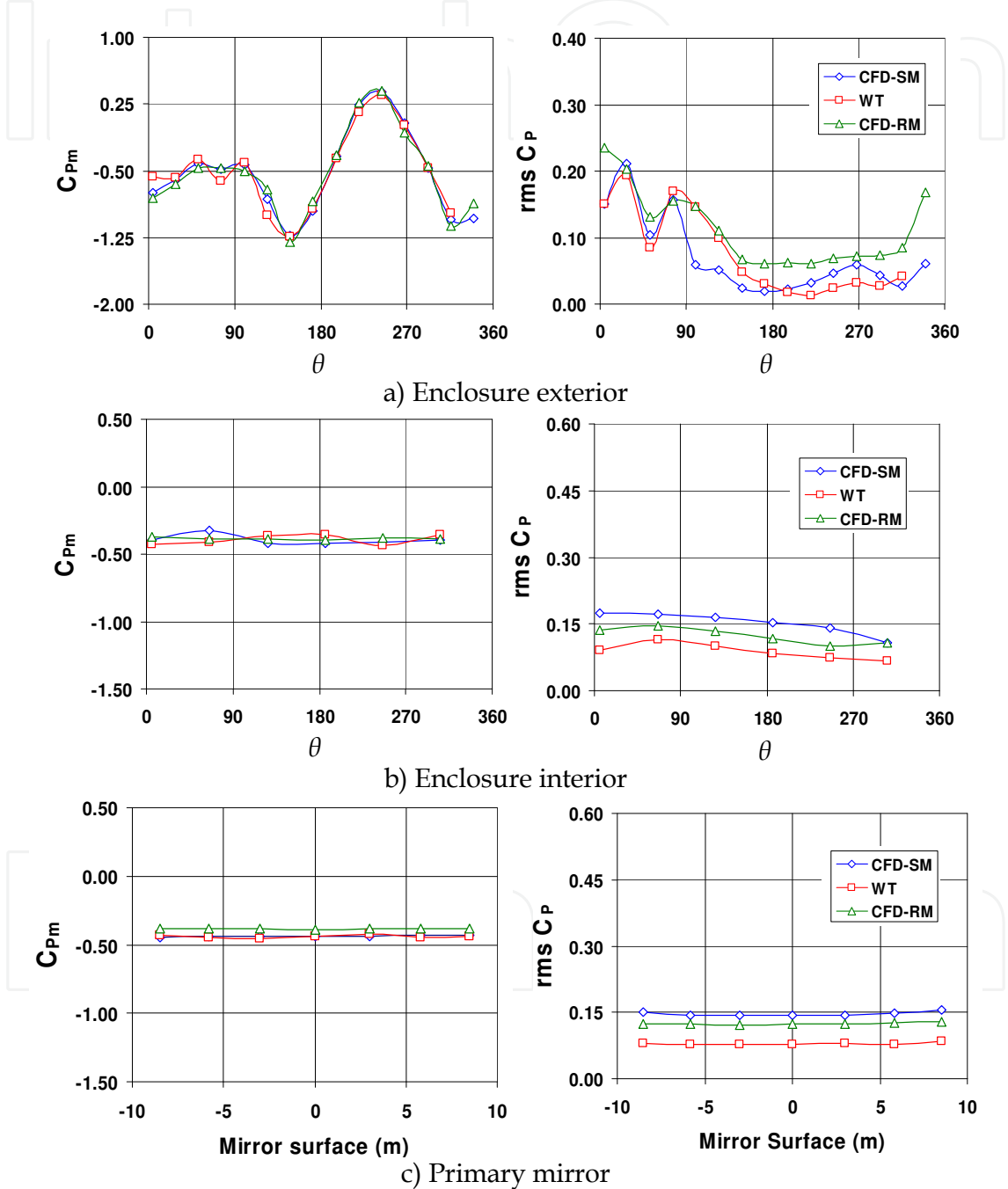
Fig. 17. Comparison between CFD and measured data: mean pressure coefficients (left) and standard deviations (right) for the Row2 pressure taps on the enclosure (a) exterior and (b) interior, and (c) the Row3 pressure taps on the primary mirror surface ($\phi = 30^\circ$ and $\varphi = 30^\circ$) (Mamou *et al.*, 2008)

As in the case of the pressure loads on the enclosure interior surface, the mean pressure over the primary mirror surface was uniform. The rms C_{Pm} values on the primary mirror were slightly overestimated by the CFD predictions. This is probably due to the three-dimensional effect of the opening free shear layer, which was not accurately simulated. Figure 17a shows two peaks of the rms C_P, which corresponded to the loci of strong and large vortices formed on the back of the enclosure, as shown in Fig. 18. The real Mach number simulation showed much better agreement with experiment for the rms C_{Pm} inside the enclosure.

Figure 19 presents a comparison between the CFD and the WT data for the C_{Pm} and the rms C_P variations on the exterior surface of the enclosure for Row2 of the pressure probes. The results were obtained for ϕ=30º and φ=0º. A good agreement between CFD and WT data was obtained for the C_{Pm}. The rms C_P trend was well captured, indicating two distinct high
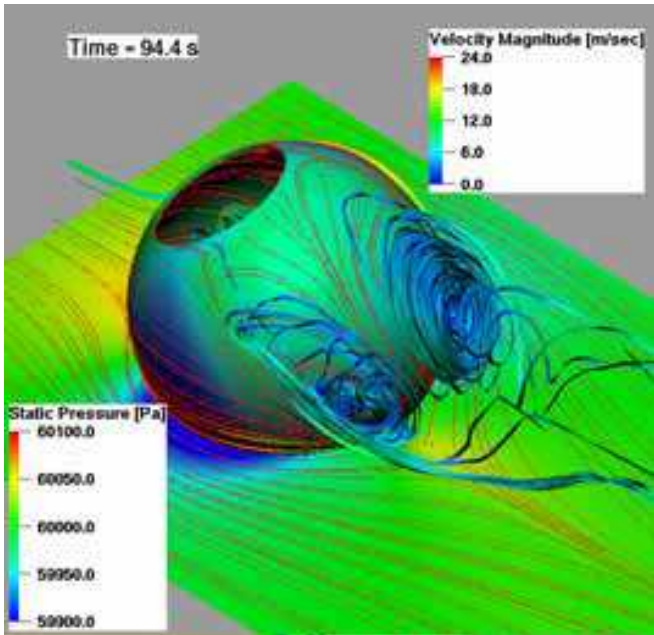
Fig. 18. Snapshot of the off-body streamlines within the separated region behind the enclosure (ϕ = 30º and φ = 30º) (Mamou et al., 2004a)
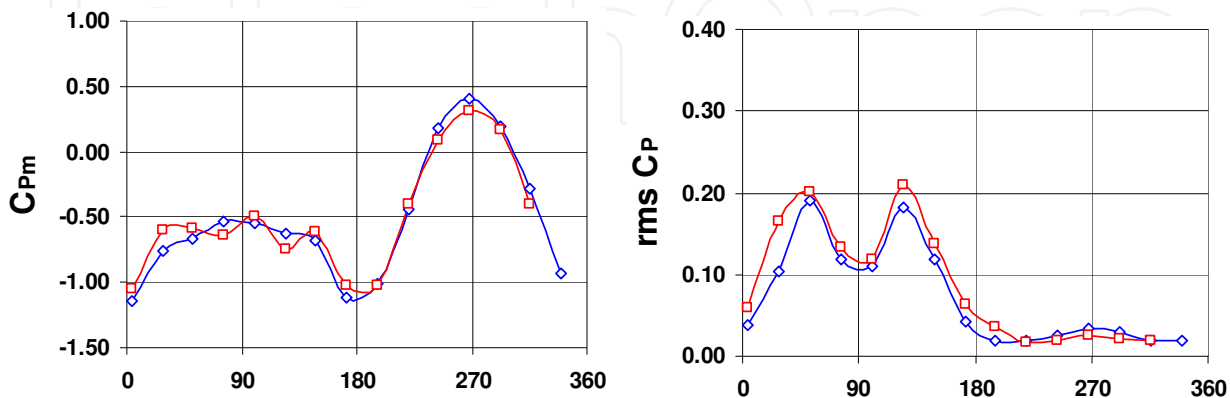
Fig. 19. Comparison between CFD and measured data: mean pressure coefficients (left) and standard deviations (right) for the Row2 pressure taps on the enclosure exterior (ϕ=30° and φ=0°) (Mamou et al., 2004a)

fluctuation peaks, which were the signature of the presence of two strong vortical flows inside the separated region $30° \leq \theta \leq 150°$. The predicted separation point for Row2 was in agreement with the mean pressure measured data and the IR measurements displayed in Fig. 9a.

For the vented enclosure configuration, the measurements revealed that the pressure tones inside the enclosure were reduced to one oscillatory mode, with a lower pressure fluctuation amplitude. Similar results were predicted by the CFD simulations performed on a 30-m full-scale telescope (Mamou *et al.*, 2004a). Only one row of vents was opened. The streamlines displayed in Fig. 19a-b show that the air flowed through the front vents and exited from the rear ones and through the enclosure opening. This obviously created a large flow circulation inside the enclosure and on the primary mirror surface, as displayed in Fig. 19b-c. The CFD results showed that, as the air flowed outwards through the enclosure opening, the free shear layer was lifted somewhat, causing less interaction with the aft edge of the opening. Also, the pressure inside the enclosure increased owing to reduced suction effects caused by the airflow through the vents.
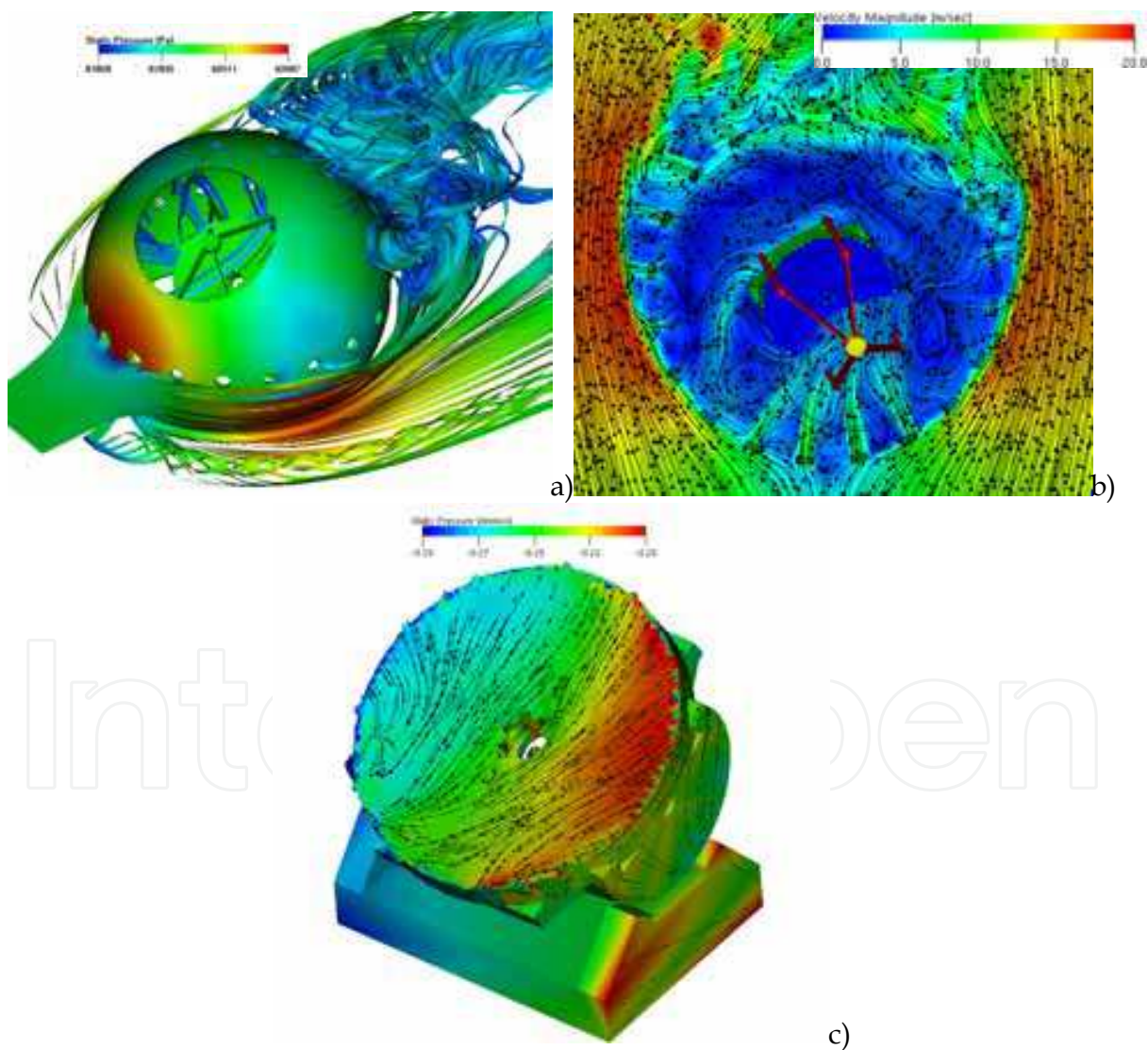

a)   b)

c)

Fig. 19. a) Off-body streamlines through the enclosure vents, b) streamlines on a horizontal cutting plane through the enclosure vents, c) streamlines on the primary mirror surface ($\phi = 30°$ and $\varphi = 30°$)

6. Conclusion

The importance of applying computational fluid dynamics (CFD) for large optical telescope flow analyses in the early design phase was emphasized and some critical challenges for accurate flow field prediction were drawn. Also, a thorough literature review was performed specifically on the role of CFD that can play towards accurate prediction of pressure loads on telescopes structure. Some recent CFD and experimental investigations, on a scaled model of a very large optical telescope housed within a spherical enclosure, were performed and led to the following remarks.

In general, when the enclosure opening was facing into the wind, both the CFD and measured data revealed that the flow was highly unsteady inside and outside the enclosure, causing unsteady wind loads on the enclosure and the telescope structure. Outside the enclosure, owing to the formation of a boundary layer over the floor, a distinct unsteady horseshoe vortex was formed. A strong shear layer was noted to evolve across the enclosure opening. The shear layer was decidedly unstable, and tended to roll up into a series of small vortices that interacted with the aft edge of the enclosure opening, resulting in large pressure fluctuations on the primary mirror surface. The mean pressure inside the enclosure was roughly uniform. The flow was separated on the back of the enclosure, starting from the aft edge of the enclosure opening towards the floor.

A spectral analysis of the pressure signal on the primary mirror surface showed the existence of at least three principal oscillatory modes. Owing to the elevated Mach number used for most of the simulations, the first CFD mode frequency was understandably under-estimated. However, when the actual wind tunnel Mach number was used in the simulations, the spectral analysis showed excellent agreement between the CFD and measured data, demonstrating the relevance of simulating appropriately the acoustic waves generated by the interaction of the shear layer vortices with the enclosure opening edge. Good comparisons were also obtained between the CFD predictions and the measurements for the mean pressure coefficients and their standard deviations around and inside the enclosure surfaces and on the primary mirror surface. For the purposes of this study, the level of agreement obtained with the experimentally observed phenomena justifies the assumption of a hydraulically smooth enclosure surface and fully turbulent flow.

Despite the good agreement between CFD and experimental results for the flow behavior inside the enclosure, the flow physics around the enclosure external surface was not properly simulated by assuming fully turbulent flows, as the infrared measurements showed a large laminar run on the front region of the enclosure, followed by transition, fully turbulent flows, and finally separated flows. Furthermore, from the smoke visualization and infrared measurements, it appeared that the flow around the enclosure was strongly affected by the tunnel floor, causing an unsteady horseshoe vortex to form, and by the enclosure opening, which disrupted the transition and separation locations expected on sphere flows in the supercritical regime. These have the effect of delaying the transition location and triggering earlier flow separation.

For bodies with a high sensitivity to the boundary layer state, such as a spherical enclosure, there is a need to simulate transition, even in the high Reynolds number case. Future work involving high Reynolds number tests and CFD simulations using hybrid and zonal DNS, LES and URANS simulations is required to address properly these flow phenomena.

7. References

Achenbach, E. (1974) The effect of surface roughness and blockage on the flow past spheres, J. Fluid Mech. (1974), vol. 65, part 1, pp 113-125.

Angeli, G.Z.; Cho, M.K.; Sheehan, M. & Stepp, L.M. (2002). Charaterization of wind loading of telescopes, SPIE procedding, Vol. 4757 "Integrated Modeling of Telescopes", Lund, Sweden, Feb. 2002, pp. 72-83.

Angeli, G.Z.; Dunn, J.; Roberts, S.; MacMynowski, D.; Segurson, A; Vogiatzis, K. & Fitzsimmons, J. (2004). Modeling tools to estimate the performance of the Thirty Meter Telescope: an integrated approach, Proceedings SPIE, Vol. 5497, pp. 237-250, 2004 Glasgow, Scotland, United Kingdom.

Babinsky, H. & Edwards, J.A. (1996) *Automatic liquid crystal thermography for transient heat transfer in hypersonic flow*, Experiments in Fluids, 21 (4) pp. 227-236, 1996.

Cho, M.K.; Stepp, L.M.; Angeli, G.Z. & Smith, D.R. (2003). Wind loading of large telescopes, Proc. SPIE, Vol. 4837, 352 (2003), Thursday 22 August 2002 , Waikoloa, HI, USA

Cho, M.K.; Stepp, L. & Kim, S. (2001). Wind buffeting on the Gemini 8m primary mirrors, Proc. SPIE 4444, 302 (2001).

Cooper, K.R.; Farrell, I.; Leclerc, G.; Franchi, G.; Vezzaro, N.; & Fitzsimmons, J. (2005). A wind tunnel test on the HIA very large optical telescope: Phase 0 - mean and unsteady pressure measurements, NRC-IAR-LR-AL-2005-0038, NRC Canada, 2005.

Cooper, K.R. & Fitzsimmons, J. (2004a). An example of cavity resonance in a ground-based structure, Fifth International Colloquium on Bluff Body Aerodynamics and Applications, Ottawa, Canada, pp. 115-118, 2004.

Cooper, K.R.; Farrell, I.; Fitzsimmons, J.; Chu, V. & Vezzaro, N. (2004b) A wind tunnel test on the HIA very large optical telescope: Phase 0 - Vented enclosure mean and unsteady mirror pressures and mean mirror loads. NRC-IAR-LR-AL-2005-0039 , NRC Canada, 2004.

De Young, D.S. (1996). Numerical simulations of airflow in telescope enclosure, *Astronomical Journal*, Vol. 112, No. 6, pp. 2896-2908

De Young, D.S. & Vogiatzis, K. (2004). Numerical simulations of airflow in very large telescope enclosures, Proc. SPIE, Second Backaskog Workshop on Extremely Large Telescopes, Vol. 5382 p. 379-387, 2004.

Hubner, J.P.; Carroll, B.F. & Schanze, K.S. (2002) Heat transfer measurements in hypersonic flow using luminescent coating techniques, Journal of Thermophysics and Heat Transfer, Vol. 16, No 4, 2002, pp. 516-522

MacMynowski, D.G.; Vogiatzis, K.; Angeli, G.Z.; Fitzsimmons, J. & Nelson, J.E. (2006) Wind loads on ground-based telescopes. *Applied Optics*, Vol. 45, No. 30, pp. 7912-7923, 20 October 2006.

Mamou, M.; Tahi, A.; Benmeddour, A.; Cooper, K.R,.; Abdallah, I.; Khalid, M. & Fitzsimmons, J. (2008). Computational fluid dynamics simulations and wind tunnel measurements of unsteady wind loads on a scaled model of a very large optical telescope. *Journal of Wind Engineering & Industrial Aerodynamics*, Vol. 96, Issue 2, pp. 257-288, ISSN

Mamou, M.; Benmeddour, A. & Khalid, M. (2004a) Computational fluid dynamics analysis of the HIA very large optical telescope: Phase 0 - full scale mean and unsteady pressure and loads predictions, NRC-IAR-LTR-AL-2004-0022, NRC Canada, 2004.

Mamou, M.; Cooper, K.R.; Benmeddour, A.; Khalid, M.; Fitzsimmons, J. & Sengupta, R. (2004b) CFD and wind tunnel studies of wind loading of the Canadian very large optical telescope, *Fifth International Colloquium on Bluff Body Aerodynamics and Applications*, Ottawa, Canada, pp. 119-122, 2004.

Mamou, M.; Tahi, A.; Abdallah, I.; Benmeddour, A. & Khalid, M. (2004c) Computational fluid dynamics analysis of the very large optical telescope – mean and unsteady pressure and loads predictions, NRC-IAR-LTR-AL-2004-0200, NRC Canada, 2004.

McCormick, B.W.: Aerodynamics, Aeronautics, and Flight Mechanics, John Wiley & Sons Edition, 1979.

Mébarki, Y. (2004) Transition detection on the iSun solar racecar from McGill University in the NRC 9-meter wind tunnel using infrared thermography, NRC LML LM-AL-2004-0081

Mébarki, Y.; Mamou, M. & Genest, M. (2009) Infrared measurements of transition location on the CRIAQ project morphing wing model. NRC-IAR-LTR-AL-2009-075.

Pottebaum, T. & MacMynowski, D.G. (2006). Wind tunnel testing of vented and unvented hemispherical telescope enclosure, J. Fluids and Structures, Vol. 22, 2006, pp. 3-19.

PowerFLOW™ explanatory notes http://www.exa.com

Quattri, M.; Koch, F.; Noethe, L.; Bonnet, A.C. & Noelting S. (2003). OWL wind loading characterization: a preliminary study, Proceedings of SPIE, Vol. 4840 Future Giant Telescopes, January 2003, pp. 459-470.

Quattri, M.; Haase, R.; Barreto Cabrera, M.; Friend Monasterio, E.; Codina, R.; Gonzalez Hernandez, M. & Reyes, M. (2008) Wind turbulence struture inside telescope enclosures. Proc. SPIE, Vol. 7017, 70170O (2008), 26 June 2008, Marseille, France.

Riewaldt., H.; McNamara, K. & Wang, X. (2004) Euro50 Wind tunnel study, Euro50 Technical Report No. 3, LUND Observatory and National University of Ireland, 2004.

Tahi, A.; Benmeddour, A.; Mamou, M. & Khalid, M. (2005a) Computational fluid dynamics analysis of the HIA 30m (TMT) very large optical telescope (VLOT) with vented enclosure: mean and unsteady pressure and loads predictions, NRC-IAR-LTR-AL-2005-0007, NRC Canada, 2005.

Tahi , A.; Benmeddour, A.; Mamou, M.; Khalid, M.; Cooper, K.R.; Fitzsimmons, J.; Freed, D. & Sengupta, R. (2005b) Computational aerodynamic analyses of different Canadian very large optical telescope configurations, AIAA-2005-5095, 23rd AIAA Applied Aerodynamics Conference, Toronto, Canada, June 2005.

Schmid, S.; Lutz, T. & Kramer, E. (2008a) Simulation of the flow around the stratospheric observatory for infrared astronomy SOFIA using URANS and DES, chapter in the Book on High Performance Computing in Science and Engineering, *Garching/Munich 2007 Publisher Springer Berlin Heidelberg* ISBN 978-3-540-69181-5, Part IV pp. 365-375, October 22, 2008.

Schmid, S.; Lutz, T.; Kramer, E. & Kuhn, T. (2008b) Passive control of the flow around the stratospheric observatory for infrared astronomy. *26th AIAA Applied Aerodynamics Conference AIAA* 2008-6717, 18 - 21 August 2008, Honolulu, Hawaii, August 2008.

Schmid, S.; Lutz, T.; Kramer, E. & Kuhn, T. (2009) Passive Control of the Flow Around the Stratospheric Observatory for Infrared Astronomy. *Journal of Aircraft*, Vol. 46, No. 4, July–August 2009.

Srinivasan, G.R. (1997) Unsteady flowfield and cavity acoustics of the stratospheric observatory for infrared astronomy. *Journal of Spacecraft and Rockets*, Vol. 34, No. 3, pp. 372-378, May–June 1997.

Srinivasan, G.R. (2000) Acoustics and unsteady flow of telescope cavity in an airplane. Journal of Aircraft Vol. 37, No. 2, pp. 274-281, March–April 2000.

Vogiatzis, K.; Segurson, A.; & Angeli, G.Z. (2004). Estimating the effect of wind loading on extremely large telescope performance using computational fluid dynamics, *Proc. SPIE Modeling and Systems Engineering for Astronomy,* Vol. 5497, pp. 311-320, 2004. Thursday 24th June 2004, Glasgow, Scotland, United Kingdom

White, F.M. (1983) Heat Transfer, Addison Wesley Educational Publishers Inc., 1983
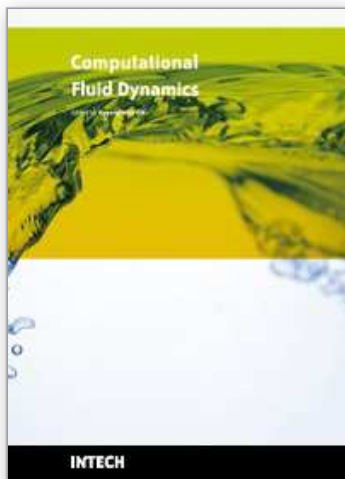
Computational Fluid Dynamics

Edited by Hyoung Woo Oh

This book is intended to serve as a reference text for advanced scientists and research engineers to solve a variety of fluid flow problems using computational fluid dynamics (CFD). Each chapter arises from a collection of research papers and discussions contributed by the practiced experts in the field of fluid mechanics. This material has encompassed a wide range of CFD applications concerning computational scheme, turbulence modeling and its simulation, multiphase flow modeling, unsteady-flow computation, and industrial applications of CFD.

How to reference

In order to correctly reference this scholarly work, feel free to copy and paste the following:

INTECH
open science | open minds